Verification and validation of blade-resolved viscous-flow tidal turbine simulations

Manuel Rentschler, Tiago Gomes, Guilherme Vaz, Luís Eça, and Stephen Turnock

Abstract—**Tidal turbines are a renewable energy source on the rise. The exceptional predictability of tidal currents contributes to a high reliability of this technology, which represents a key advantage in the endeavor to become a major contributor to the energy mix. To foster the development and to support the design process of tidal turbines, reliable numerical modeling techniques are required. This paper presents verification and validation work performed within the framework of the Supergen ORE Tidal Turbine Benchmarking Study. Viscous-flow CFD code ReFRESCO is used to conduct blade-resolved simulations of the towing tank experiments. In a first approximation, a steady-state frozen-rotor approach is chosen. A transition model, γ-Re_θ, is employed to predict the flow state transition on the turbine blades. In the process, the sensitivity to input turbulence quantities is highlighted. The numerical uncertainty is estimated based on mesh refinements. Finally, a conclusion is drawn to which accuracy the presented numerical models can predict the outcome of the experiments.**

Index Terms—**Computational Fluid Dynamics, Verification & Validation, Tidal Current Turbine, Frozen-Rotor Approach**

I. Introduction

THE extraction of tidal energy through marine current turbines has experienced a surge of interest around the turn of the millennium [1]. With the European Marine Energy Centre (EMEC) the world's first wave and tidal test center was established in 2003. Because prototype testing in real-world conditions was (and still is) very expensive though, experimental model testing in water tanks, as already common for marine propellers, represented an alternative solution. A popular example that motivated a lot of follow-up research are the tidal turbine experiments that were conducted at University of Southampton [2], [3]. Typically much less expensive than experimental model testing is numerical modeling. While in the beginning less computationally complex methods like Blade Element Momentum Theory were favored [4], growing computational resources allowed couplings with Computational Fluid Dynamics (CFD) [5] and finally fully blade-resolved CFD simulations [6], [7]. Despite recent research efforts [8]–[10] unsteady phenomena and loading for off-design conditions are not sufficiently well understood to this day and a lack of confidence in CFD numerical predictions still persists. This sparked the motivation for the Supergen ORE Tidal Benchmarking Study [11], [12]. The present work resulted from a blind test contribution to the first stage of the benchmarking. Unsteady effects are not yet considered here. Instead, the comparatively efficient steady-state frozen-rotor approach was used to test different numerical setups, to assess the sensitivity to input parameters, perform a solution verification, and to provide a first estimation for the credibility of the simulations.

The remainder of this work is structured as follows: In section II, the mathematical model behind the numerical approach is introduced. In section III, the numerical setup is explained, covering numerical solution methods, the computational domain and meshes, and the simulated test cases. Simulation results are presented in section IV. Firstly, suitable inlet turbulence quantities are identified through turbulence decay simulations, then a verification study is conducted to estimate numerical uncertainties and finally the simulation results are compared to the experimental data. A summary of the most important findings and suggestions for future work are ultimately given in section V.

II. Mathematical model

A. RANS equations

The governing equations are the incompressible Navier-Stokes equations following the principle of conservation of mass and momentum. To describe the turbulent flow, a Reynolds-averaging is applied, splitting the instantaneous quantities into time-averaged and fluctuating components and time-averaging the equation, which yields the Reynolds-Averaged Navier-Stokes (RANS) equations

$$\frac{\partial \overline{u}_i}{\partial x_i} = 0\,, \tag{1}$$

$$\frac{\partial(\rho\overline{u}_i)}{\partial t} + \frac{\partial(\rho\overline{u}_i\overline{u}_j)}{\partial x_j} = -\frac{\partial \overline{p}}{\partial x_i} + \frac{\partial}{\partial x_j}\left(\mu\left(\frac{\partial \overline{u}_i}{\partial x_j} + \frac{\partial \overline{u}_j}{\partial x_i}\right) - \rho\overline{u_i' u_j'}\right) + \rho\overline{f}_i\,, \tag{2}$$

The first author received financial support from a studentship granted by Fundação para a Ciência e a Tecnologia (FCT) with the reference 2021.04948.BD.

M. Rentschler, T. Gomes and G. Vaz are affiliated with blueOASIS–Blue Ocean Sustainable Solutions, Ericeira Business Factory, R. Prudêncio Franco da Trindade 4, 2655-344 Ericeira, Portugal (e-mail: mrentschler@blueoasis.pt).

L. Eça is affiliated with Instituto Superior Técnico, University of Lisbon, Av. Rovisco Pais, 1049-001 Lisbon, Portugal (e-mail: luis.eca@tecnico.ulisboa.pt).

S. Turnock is affiliated with Department of Civil, Maritime and Environmental Engineering, University of Southampton, University Rd, Southampton SO17 1BJ, United Kingdom (e-mail: S.R.Turnock@soton.ac.uk).

Digital Object Identifier:
https://doi.org/10.36688/ewtec-2023-316

both in index notation. Herein, ρ denotes the density, t the time, u the velocity, p the pressure, μ the dynamic viscosity, and f the body force. Time-averaged quantities are indicated by an overbar, fluctuating quantities by a tick. Assuming steady flow, the unsteady term disappears, but for completeness it is printed here and in the following transport equations.

The contributions of the turbulent small scales $\rho\overline{u_i' u_j'}$, represented in the so called Reynolds stress tensor, need to be additionally modeled to close the system of equations. A popular modeling approach is the Boussinesq approximation [13] which reduces the problem to determine the six unknown Reynolds stresses to finding a suitable expression for a parameter denoted eddy viscosity. The calculation of this expression is the objective of the turbulence model introduced below.

B. Turbulence model

In this work, the k-ω SST turbulence model developed by Menter et al. [14] is employed across all simulations. The turbulence model adds two more equations to solve. The transport equations for the turbulent kinetic energy k and specific dissipation rate ω, again in conservation form, and for completeness including the unsteady term, read

$$\frac{\partial(\rho k)}{\partial t} + \frac{\partial(\rho u_j k)}{\partial x_j} = P_k - D_k + \frac{\partial}{\partial x_j}\left((\mu + \sigma_k \mu_t)\frac{\partial k}{\partial x_j}\right), \quad (3)$$

$$\frac{\partial(\rho\omega)}{\partial t} + \frac{\partial(\rho u_j \omega)}{\partial x_j} = P_\omega - D_\omega + \frac{\partial}{\partial x_j}\left((\mu + \sigma_\omega \mu_t)\frac{\partial \omega}{\partial x_j}\right) + 2(1-F_1)\frac{\rho\sigma_{\omega_2}}{\omega}\frac{\partial k}{\partial x_j}\frac{\partial \omega}{\partial x_j}. \quad (4)$$

Both equations contain the eddy viscosity μ_t, a parameter which was first introduced by Boussinesq [13]. In Menter's SST turbulence model it is reexpressed as function of k and ω according to

$$\mu_t = \frac{\rho a_1 k}{\max(a_1\omega, SF_2)}, \quad (5)$$

where S is the magnitude of the strain-rate tensor. For the further auxiliary functions and coefficients refer to the original paper of the turbulence model [14].

C. Transition model

At moderate Reynolds numbers, the flow around air-/hydrofoils exhibits both laminar and turbulent regions. In such conditions, commonly used turbulence models tend to underestimate the extent of the laminar area, predicting transition to fully turbulent flow too close to the leading edge of the foil [15]. The addition of a dedicated transition model promises to correct that behavior. In this work, the local correlation-based γ-Re_θ transition model is deployed. It was originally developed by Langtry and Menter [16] for use in combination with the k-ω SST turbulence model. More recently, the transition model has also been coupled to other turbulence model implementations such as the k-$\sqrt{k}L$ model [15], [17].

The transition model adds two further transport equations, one for the intermittency γ and another for the local transition momentum thickness Reynolds number $\widetilde{Re}_{\theta_t}$:

$$\frac{\partial(\rho\gamma)}{\partial t} + \frac{\partial(\rho u_j \gamma)}{\partial x_j} = P_\gamma - D_\gamma + \frac{\partial}{\partial x_j}\left(\left(\mu + \frac{\mu_t}{\sigma_f}\right)\frac{\partial \gamma}{\partial x_j}\right), \quad (6)$$

$$\frac{\partial(\rho\widetilde{Re}_{\theta_t})}{\partial t} + \frac{\partial(\rho u_j \widetilde{Re}_{\theta_t})}{\partial x_j} = P_{\theta_t} + \frac{\partial}{\partial x_j}\left(\sigma_{\theta_t}(\mu + \mu_t)\frac{\partial \widetilde{Re}_{\theta_t}}{\partial x_j}\right). \quad (7)$$

Those equations interact with the turbulence model through a modification of the production and destruction term in the transport equation of the turbulent kinetic energy k as well as the blending function. For a detailed description of the source terms, the values of the constants, and the modifications to the turbulence model view [16].

D. Rotation modeling

For the modeling of the rotor motion of the tidal turbine, a moving reference frame technique is chosen. Therein, a non-inertial coordinate system is assumed to rotate with constant angular velocity Ω relative to the inertial earth-fixed coordinate system. While the rotor itself does not move and stays in the position as defined by the fixed mesh (hence also the denomination frozen-rotor approach), the rotation is imposed on the flow by adding a body force term on the right-hand side of the momentum equation. For the absolute velocity formulation (AF) used in this work, the term reads

$$\vec{f}_{AF} = \vec{\Omega} \times \vec{u}. \quad (8)$$

The advantage of this motion modeling approach lies in the reduction of computational time, being able to run the simulations in steady state. Meanwhile, for the steady solution a fully developed flow is assumed, transient effects are not captured. A further limitation is that no relative motion between moving and fixed bodies can be modeled. Consequently, the geometry needs to be restricted to the rotating part. Details regarding the numerical setup including the modeled geometry, the computational domain and the meshes are presented in the following section.

III. Numerical setup

A. CFD software

To solve the previously introduced mathematical problem numerically, CFD code ReFRESCO [1] is employed. The software is a community-based, open-usage, viscous-flow CFD code developed for maritime

[1] https://www.marin.nl/en/facilities-and-tools/software/refresco

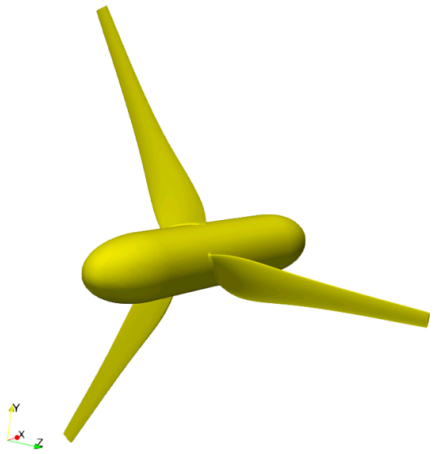

Fig. 1. Modeled turbine geometry

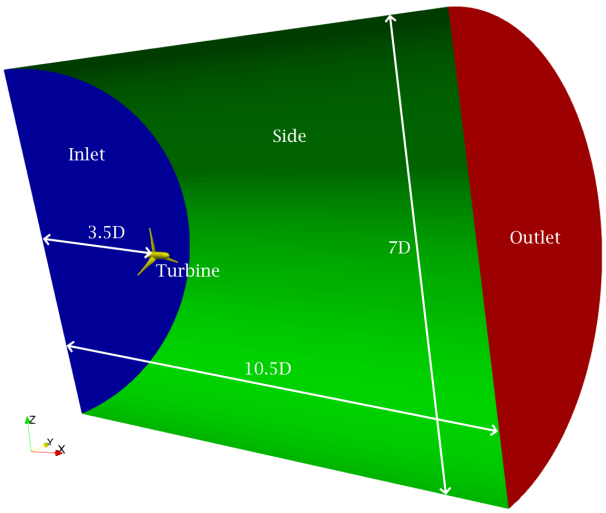

Fig. 2. Computational domain

applications. It solves multi-phase, unsteady, incompressible, viscous flows using the Navier-Stokes equations, integrating turbulence models, cavitation models and volume-fraction transport equations for different phases [18]. The equations are discretized using a finite-volume approach with cell-centered collocated variables, in strong-conservation form. A pressure-correction equation based on the SIMPLE algorithm is used to ensure mass conservation [19]. The applied numerical schemes are specified in Table I and of second-order accuracy, except for the first-order upwind convection schemes.

B. Turbine geometry

A detailed description of the experiments forming the validation basis of the tidal turbine benchmarking study is provided on the official project homepage [2], the geometry of the turbine is available as free download. The three-bladed rotor has a diameter of $D = 1.6\,\mathrm{m}$, the rotating cylindrical part of the nacelle has a diameter of $0.2\,\mathrm{m}$. The original geometry includes a lengthy non-rotating nacelle part and the tower structure, which are both neglected in the present simulations in favor of the frozen-rotor approach (see section II-D). To avoid sharp edges at the cut nacelle, the rounded hub is mirrored to the downstream side. The total nacelle length of the modeled geometry is $0.9\,\mathrm{m}$. The final turbine geometry used for the simulations is shown on Fig. 1.

The blades are entirely based on the NACA 63-415 profile. Meanwhile, the profile is modified by a thickening function that removes the sharp trailing edge to facilitate numerical modeling but at the same time preserves the performance of the turbine.

C. Computational domain

The turbine is placed into a cylindrical domain with a diameter of $7D$ and a total length of $10.5D$. The distance from the inlet to the rotor plane is $3.5D$. The arrangement is pictured on Fig. 2. Based on previous simulation exercises, those dimensions are large enough so that the boundary conditions at the side and outlet of the domain do not influence the flow around the turbine. Note that this differs from the experimental setup, in which the turbine structure is placed in a large rectangular towing tank, but the tip clearance to the free surface only amounts to about $0.22D$. The influence of the free surface and unsteady loading due to waves will be investigated in a later stage of the benchmarking study. The fluid properties from the experimental campaign are given with a water temperature of $12.97\,^{\circ}\mathrm{C}$, a density of $999.4\,\mathrm{kg\,m^{-3}}$, and a dynamic viscosity of $1.26 \times 10^{-3}\,\mathrm{Pa\,s}$.

Regarding the boundary conditions, at the outlet an outflow condition is applied, prescribing zero normal derivatives for all flow variables. At the side, a pressure boundary condition is used, where also zero normal derivatives are enforced except for the static pressure which is set to a user specified reference value, here $p_{\mathrm{ref}} = 0$. On the turbine, a no-slip wall condition is employed, imposing a zero velocity relative to the surface, the turbulent kinetic energy k is equally set to zero, the dissipation rate ω is set to the near-wall analytic solution, and for the remaining flow variables zero normal derivatives are enforced. At the inlet, an inflow condition is prescribed, requiring specification of inflow velocities and inlet turbulence quantities, the intermittency γ is set to unity, and the momentum thickness Reynolds number $\widetilde{Re}_{\theta_t}$ is calculated from the turbulence intensity [20].

D. Test cases

Two different experimental conditions are to be considered. Firstly the *clean* cases, for which the uniform inflow speed is set to $u_{\mathrm{ref,clean}} = 1\,\mathrm{m\,s^{-1}}$, coinciding with the tow speed. Meanwhile, the inherently low turbulence levels in the towing tank motivated to conduct a second set of test cases with a turbulence grid installed in front of the rotor. The grid is not only responsible for elevated turbulence levels, but also a reduction in streamwise velocity at the rotor plane. Hence, for the *grid* cases, the inflow speed is set to $u_{\mathrm{ref,grid}} = 0.9207\,\mathrm{m\,s^{-1}}$. The target turbulence quantities

[2]https://supergen-ore.net/projects/tidal-turbine-benchmarking

TABLE I
NUMERICAL SCHEMES

Equation	Solver	Preconditioner	Convection scheme	Diffusion scheme	Gradient scheme
Momentum	GMRES	Jacobi	Limited QUICK	Central Differencing	Gauss
Pressure	CG	Block-Jacobi	–	–	Gauss
Turbulence	GMRES	Block-Jacobi	First Order Upwind	Central Differencing	Gauss
Transition	GMRES	Block-Jacobi	First Order Upwind	Central Differencing	Gauss

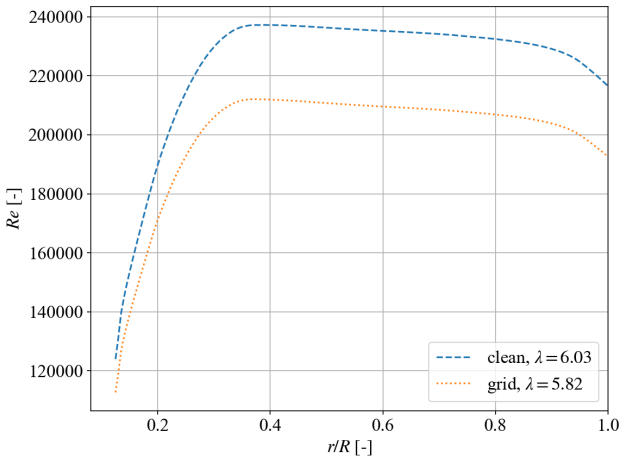

Fig. 3. Local Reynolds number along the turbine blade for an intermediate tip speed ratio λ

at the rotor plane are a turbulence intensity of $I = 3.1\,\%$ and an integral length scale of $l = 0.037\,\mathrm{m}$. However, due to turbulence decay the turbulence intensity to be specified at the inlet needs to be higher than the target value. The determination of a suitable inlet turbulence intensity is the objective of the numerical turbulence decay tests presented in section IV-A. The radial distribution of the local chord-based Reynolds number at the turbine blades resulting from the two inflow speeds and an intermediate tip speed ratio of $\lambda \approx 6$ is shown on Fig. 3. Values well below 3×10^5 are revealed, which lie within the critical Reynolds number regime where laminar-turbulent transition plays a substantial role in the flow [21].

E. Meshes

The computational meshes are created with commercial software Hexpress [3], an unstructured hexahedral mesh generator. In order to determine the discretization error from a mesh refinement study, see section IV-B, at least four increasingly refined, geometrical similar meshes are recommended [22]. For unstructured meshing of complex geometries, the condition of geometric similarity can usually be fulfilled only approximately. A guide on best practices is given by Crepier [23].

The characteristics of the meshes generated for the present study following those guidelines are tabulated in Table II. The thin trailing edge and fillets of the blades represent a challenge to create a relatively coarse

[3]https://www.numeca.com/product/omnis-hexpress

TABLE II
MESH PROPERTIES FOR DIFFERENT REFINEMENTS

	Ref 1	Ref 2	Ref 3	Ref 4
Refinement factor	1	1.5	2	2.5
No. diffusion layers	2	3	4	5
First layer thickness [µm]	7.25	4.56	3.32	2.61
VL stretching ratio	1.4	1.25	1.18	1.14
No. viscous layers	10	15	20	25
No. cells [$\times10^6$]	**3.3**	**9.1**	**19.1**	**34.3**
Min. orthogonality [°]	4	8	5	5
Max. skewness	0.96	0.94	0.94	0.93

mesh. With lots of local refinement necessary, even the coarsest mesh achieves a cell count of over 3×10^6. The finest discretization reaches a total of over 34×10^6 cells.

Note how, according to geometric similarity, the refinement factor is a proportionality constant for the number of diffusion and viscous layers (not for the first layer thickness and the stretching ratio though, see explanation in [23]). The numbers as indicated in the table are only indicative for the meshes generated, as Hexpress may adapt them slightly during the meshing process, a tradeoff to improve mesh quality. The values of the first layer thickness are chosen with the aim to achieve a non-dimensional wall distance of $y^+ < 1$ to resolve the viscous sublayer of the boundary layer even for the coarsest mesh. An overview of the meshes on the surface of the turbine and around a foil section is depicted on Fig. 4 and 5 for the coarsest and finest discretization, respectively.

Two mesh quality parameters are also listed in Table II, the minimum orthogonality and the maximum skewness. For ReFRESCO, the aim usually is to keep the values above $10°$ and below 0.9, respectively. None of the meshes fulfills those target values. The amount of problematic cells is not very large though and is a lower three-digit figure for the coarsest mesh and only a few dozens for the finest mesh. Critical locations are confined to selected spots at the trailing edge and fillets. This issue did not lead to any critical failure of the simulations.

IV. RESULTS

A. Turbulence decay

As mentioned earlier, the inflow boundary condition requires the specification of turbulence quantities at the inlet. One parameter to be prescribed is the turbulence intensity I, that is defined as the ratio of the root-

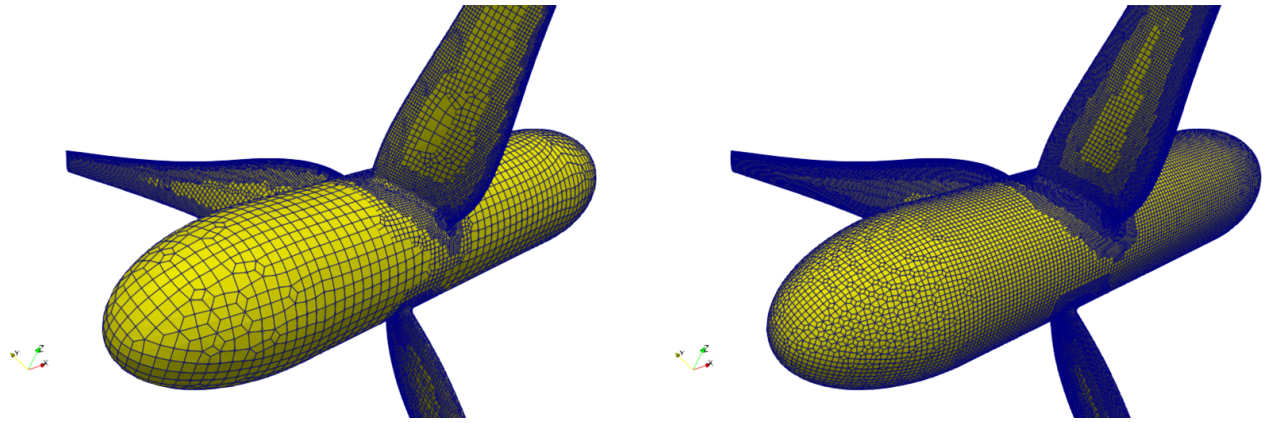

(a) Ref 1 mesh (b) Ref 4 mesh

Fig. 4. Surface mesh of the turbine

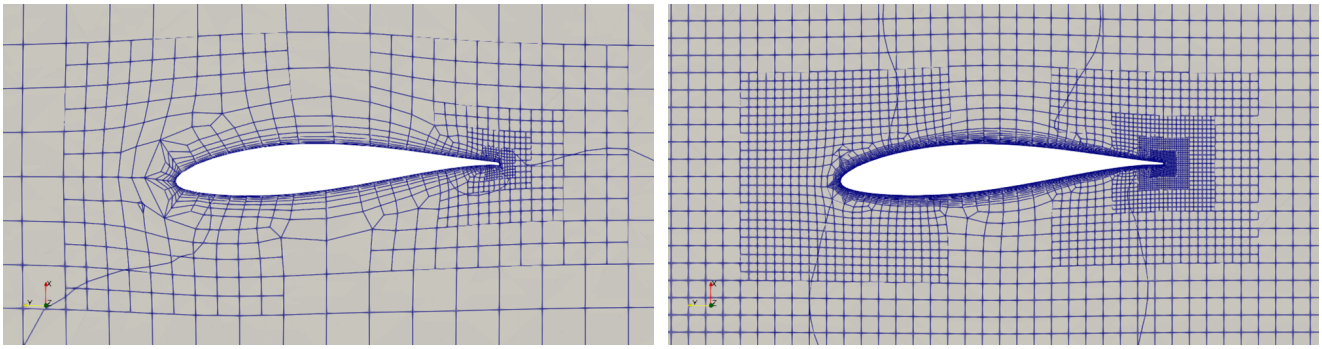

(a) Ref 1 mesh (b) Ref 4 mesh

Fig. 5. Mesh around foil section

mean-square of the turbulent velocity fluctuations u' and mean velocity U:

$$I = \frac{u'}{U}\,. \tag{9}$$

The velocity fluctuations are related to the turbulent kinetic energy k through

$$u' = \sqrt{\frac{1}{3}(u_x'^2 + u_y'^2 + u_z'^2)} = \sqrt{\frac{2}{3}k}\,. \tag{10}$$

The $k-\omega$ turbulence model is known for a strong decay of turbulence quantities in the freestream. At the same time, transition models are sensitive to those parameters [24]. A correct specification of the turbulence quantities is therefore imperative. To choose the turbulence inlet conditions for the present test cases, a parametric study is conducted and the turbulence decay is investigated. Because the turbulence intensity at the rotor plane was measured in the experiments in absence of the turbine, the numerical simulations are run for an empty domain of the finest discretization Ref 4.

Besides the turbulence intensity, ReFRESCO takes a second parameter at the inlet, the eddy viscosity ratio μ_t/μ. Fig. 6 shows the turbulence decay at the center line of the domain when default values are applied, that is $I = 1\,\%$ and $\mu_t/\mu = 1$. A steep drop in I is already observed for the first cell (hence the curve not starting at $1\,\%$). The steepness of the decay curve

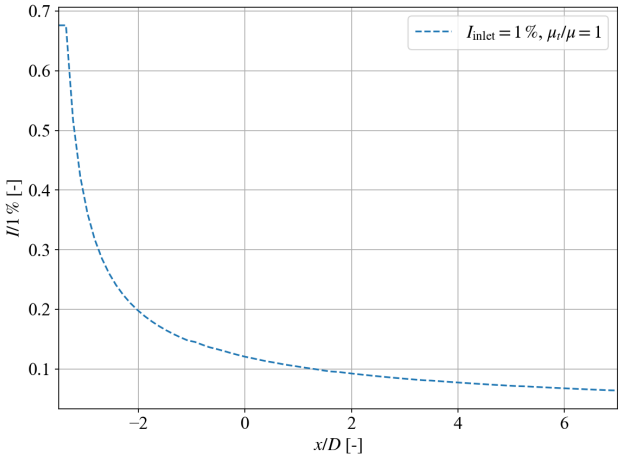

Fig. 6. Turbulence decay for an inlet turbulence intensity of $1\,\%$

reduces towards the outlet, but overall the curve is monotonically decreasing. At the rotor plane, I is just above $0.1\,\%$.

For the test cases with elevated turbulence level due to the turbulence grid, an experimentally measured $I = 3.1\,\%$ at the rotor plane is aimed for. To avoid extremely high inlet turbulence quantities and limit their decay, two measures are taken. Firstly, until $1D$ in front of the rotor plane, the turbulence quantities are frozen by ignoring the dissipation term in the transport equations

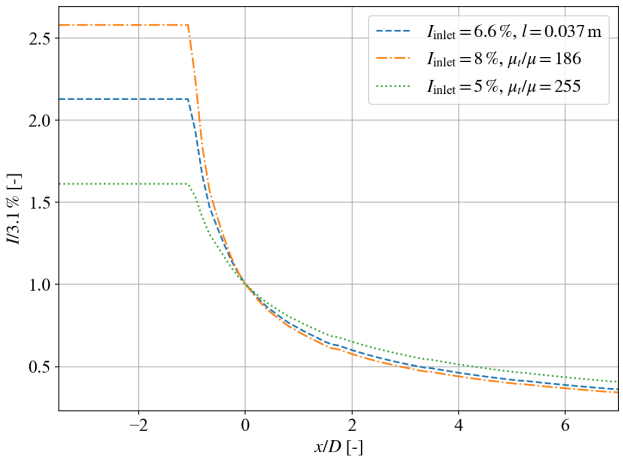

Fig. 7. Turbulence decay for different inlet value combinations

of the turbulence model [15]. Secondly, the decay rate is altered by choosing increased values for the eddy viscosity ratio [25]. The dependence of the turbulence decay behavior on multiple parameters leads to the situation that different combinations of parameters can yield the required I at the desired location. Fig. 7 exemplarily shows three of those combinations (note the normalized y-scale). Summarizing, a higher eddy viscosity ratio allows for a lower inlet I. The middle curve corresponds to a setup in ReFRESCO in which, instead of the eddy viscosity ratio, the turbulence length scale l was prescribed, which is available from the experiments. Extraction from the flow field data reveals that the corresponding $\mu_t/\mu = 204$ and thus as expected the corresponding decay curve lies in between the other two cases. Ultimately, it is found that all three options that achieve the target I at the rotor plane yield identical turbine loads, e.g. the thrust and power coefficients differ less than $1\,‰$In the following, all *grid* cases with elevated turbulence refer to the version with $I = 6.6\,\%$ and $l = 0.037\,\text{m}$.

B. Solution verification

Solution verification aims at estimating the numerical uncertainty of a simulation result whose exact solution is, usually, not known. Commonly, the numerical error consists of the sum of the round-off error, the iterative error and the discretization error. The round-off error originates from the incapability of computers to represent real numbers with infinite accuracy. However, for computations with double precision, the round-off error may be neglected.

The iterative error arises from the solution procedure of the non-linear system of equations governing the flow. A common quantity to estimate the iterative error are the residuals of the flow field variables. However, as in the benchmarking the validation data focuses on the turbine loads, the iterative changes of the power and thrust coefficient are considered in this work. The coefficients are determined from the axial torque M_x and force F_x, respectively, according to

$$C_P = \frac{M_x \Omega}{\frac{1}{2}\rho u_{\text{ref}}^3 \frac{1}{4}\pi D^2}\,, \tag{11}$$

$$C_T = \frac{F_x}{\frac{1}{2}\rho u_{\text{ref}}^2 \frac{1}{4}\pi D^2}\,. \tag{12}$$

The relative iterative changes of the coefficients $|C_i - C_{i-1}|/C_i$ for clean and grid cases are shown on Fig. 8. The graphs correspond each to the finest discretization Ref 4 and an intermediate tip speed ratio $\lambda \approx 6$. In the *clean* case the changes remain below 1×10^{-5} in the second half of simulation time. For the grid case the changes stagnate at even lower levels. In the following it is demonstrated, that the iterative error is at least two orders inferior to the discretization error, and therefore may be deemed negligible in the numerical uncertainty estimation [26].

The methodology and theoretical background for determining the discretization error based on grid refinement studies is explained in detail by Eça and Hoekstra [22]. In short, the results for an evaluation parameter ϕ are plotted over the relative step size, a non-dimensional discretization parameter. In the present work, the step size results from the ratio of the number of surface cells of the rotor of a certain mesh to the corresponding value of the finest mesh. Then, a least squares fit is applied in order to extrapolate the solution at step size 0 for a, theoretically, infinitesimal fine discretization. Depending on the observed order of convergence and the difference between actual and extrapolated result the uncertainty U_ϕ is determined for each discretization, also taking into account a safety factor and the standard deviations of the fit. The unknown exact solution is then expected in the interval

$$\phi_i - U_\phi \leq \phi_{\text{exact}} \leq \phi_i + U_\phi\,. \tag{13}$$

Above described procedure to determine the discretization error is implemented into the *Verification Tools* software available from the homepage of *MARIN* research institute [4]. The discretization uncertainty estimation of thrust and power coefficient for the *grid* case at $\lambda \approx 6$ is plotted on Fig. 9. For C_T, the fitted curve decreases monotonically from larger step size (coarser mesh) to smaller step size (finer mesh). At the same time, the size of the error bars decreases towards smaller step size. As is to be expected, the extrapolated value of the exact solution lies within the error bars. For the finest discretization, the uncertainty has a value of just above $3\,\%$. Regarding C_P, the results from the different meshes lie relatively close together, but are not organized monotonically as for C_T. The slope of the resulting fitting curve increases towards step size 0 and thereby a relatively large uncertainty of over $13\,\%$ is obtained even for the finest mesh. While the fit chosen by the software may be the most suitable from mathematical point of view, it is questionable in terms of CFD perspective. Arguably, a linear extrapolation would have been a better choice in this non-monotonic scenario, and would have resulted in a smaller uncertainty. In the future, also an even finer mesh can be considered to obtain more data points for the fit.

For the *clean* case, the uncertainty extrapolations for the coefficients look very similar and thus are not

[4] https://www.marin.nl/en/research/free-resources/verification-and-validation/verification-tools

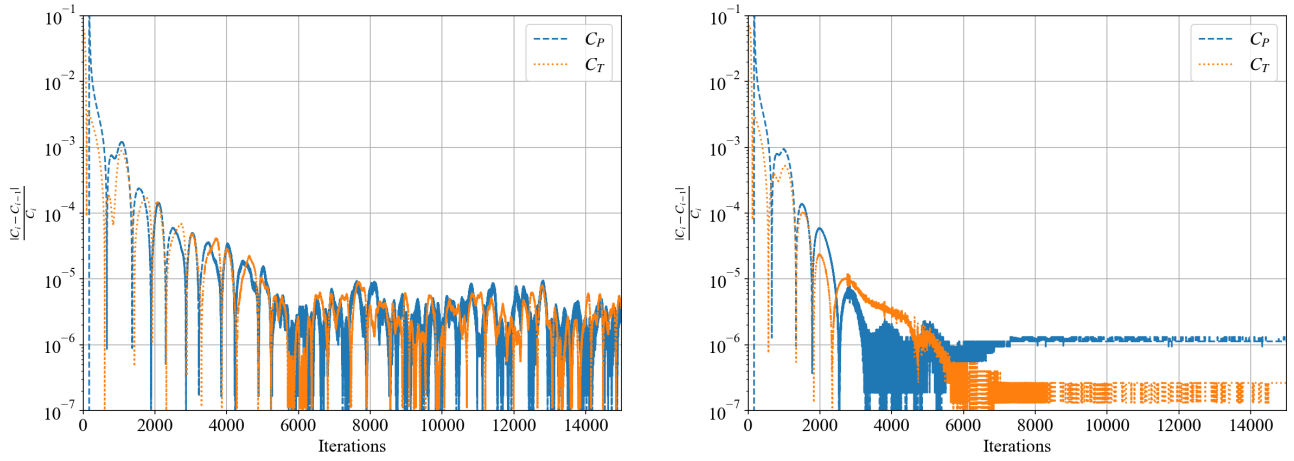

(a) *Clean* case (b) *Grid* case

Fig. 8. Iterative changes of power and thrust coefficient

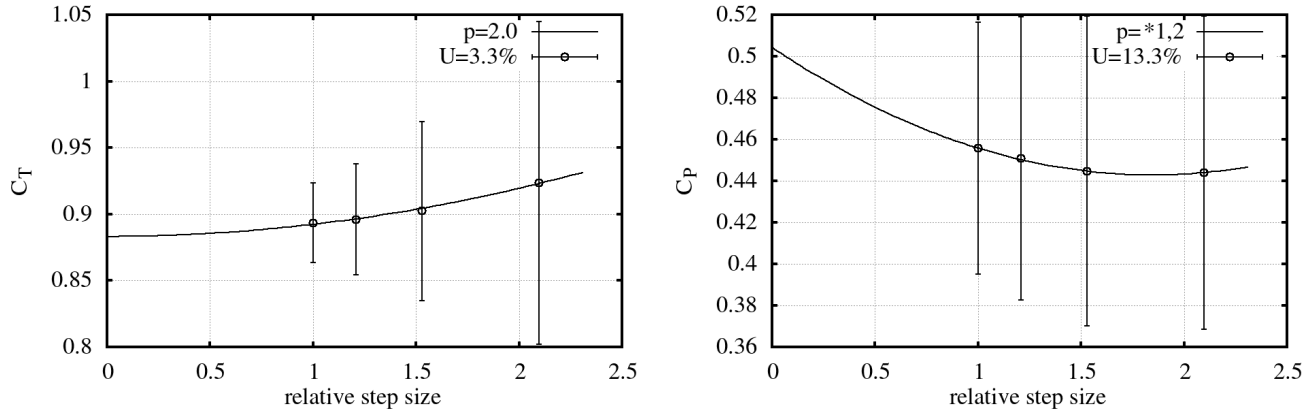

(a) C_T (b) C_P

Fig. 9. Discretization error estimation for *grid* case

TABLE III
DISCRETIZATION ERROR FOR FINEST MESH REF 4, $\lambda \approx 6$

	U_{C_T} [%]	U_{C_P} [%]
Clean case	5.1	13.3
Grid case	3.3	13.3

shown here. Meanwhile, all the uncertainties of the finest mesh are contained in Table III. For C_T the achieved discretization error is around $5\,\%$ and thus slightly higher than in the *grid* case, for C_P a similar error is observed. The conclusion of the verification exercise is that the discretization error is by far the most dominant compared to round-off and iterative error.

C. Validation

The simulation results are now compared to experimental results. Thrust and power coefficients for the *clean* cases are plotted over a range of tip speed ratios λ on Fig. 10. For the intermediate λ, the previously determined numerical uncertainty is visualized by bars. C_T is slightly underpredicted by the simulations towards lower λ and slightly overpredicted at higher λ. Meanwhile, the experimental result lies well within the numerical uncertainty error bars. For a complete validation, also the experimental uncertainty should be considered. However, at the time of writing the data is not published yet. For C_P, all the simulation results are underpredicted compared to the experiments. This is especially true for lower λ, where the difference to the experimental results exceeds $10\,\%$.

The thrust and power coefficients of the *grid* cases with elevated ambient turbulence level are shown on Fig. 11 for a range of operational conditions of the turbine. The overprediction of C_T at intermediate and higher λ amounts to $5\,\%$ and more and is thus more pronounced than in the *clean* cases. Also, the experimental result lies outside of the numerical uncertainty interval. However, considering a certain experimental uncertainty, an overlap of the solution ranges seems likely. Regarding C_P, the *grid* cases agree better with the experiment than in the *clean* cases. The differences are well below $5\,\%$, the only exception being the lowest simulated λ.

To further analyze the different simulated behavior of *clean* and *grid* cases the limiting streamlines on the suction side of the turbine blade are compared on Fig.

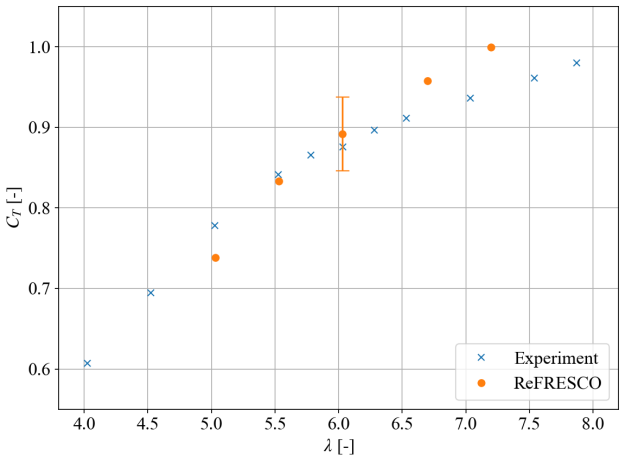

(a) C_T

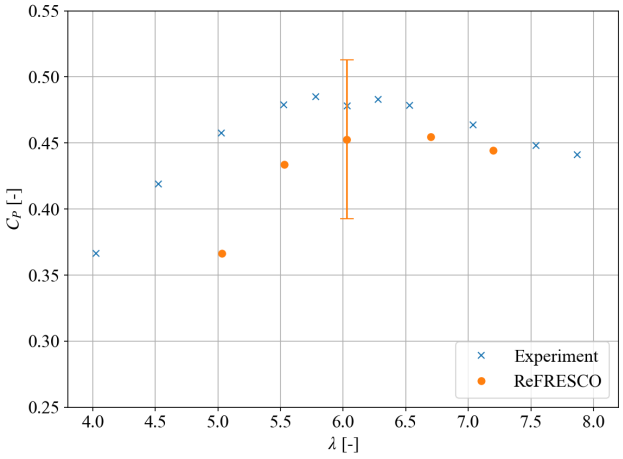

(b) C_P

Fig. 10. Comparison of thrust and power coefficients for *clean* cases

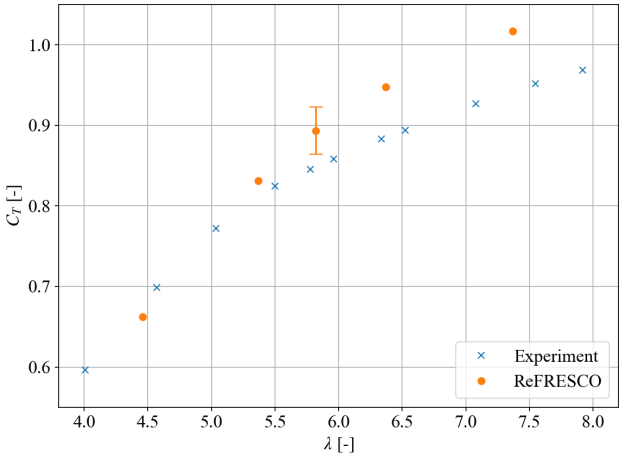

(a) C_T

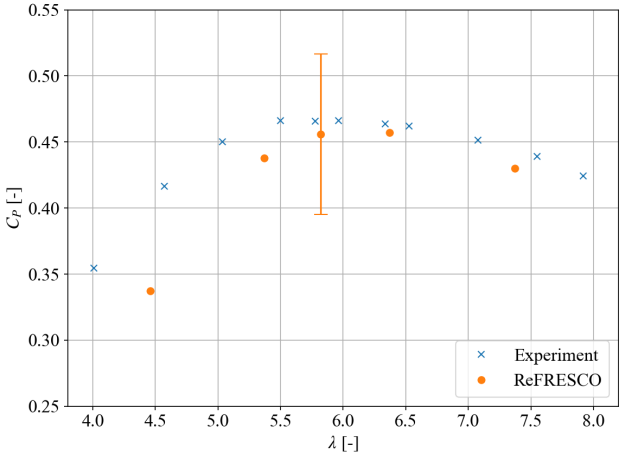

(b) C_P

Fig. 11. Comparison of thrust and power coefficients for *grid* cases

12. This visualization makes it possible to identify flow separation lines, here roughly sketched by a red line. The plots correspond to the intermediate tip speed ratio $\lambda \approx 6$, the leading edge of the blade is at the bottom, the trailing edge at the top. In the *clean* case a first separation line is identified at around $40\,\%$ of the chord length. Behind the first separation line, the flow conditions look quite chaotic, and smaller regions in which flow attaches and detaches again are observed. Meanwhile, for the *grid* case, the separation region is a lot smaller and is limited to a thin band along the trailing edge. Because the identical numerical setup is used in the two cases and similar tip speed ratios are compared, the different separation behavior can only be traced back to the difference in turbulence levels. Accordingly, the more turbulent flow tends to withstand the adverse pressure gradient along the chord for longer than the less turbulent flow. Thus, a higher ambient turbulence intensity leads to the observed reduction of the separation zone. To conclude, the findings of this work are summarized in the next section.

V. Conclusions

This work presented a steady-state frozen-rotor RANS approach to simulate towing tank experiments of a tidal turbine. The thrust and power coefficients were evaluated over a range of tip speed ratios in two scenarios comprising the *clean* setup with low ambient turbulence and the *grid* setup with elevated turbulence. The numerical uncertainty of the hydrodynamic coefficients was estimated from grid refinement studies and considered to judge the credibility of the simulations in comparison with the experimental data.

One of the most important findings of this work is the importance to accurately define the inlet turbulence quantities and consider their decay behavior. The freezing of turbulence quantities at the beginning of the domain proved to be effective to avoid excessive decay. Moreover, the eddy viscosity ratio can be instrumentalized to regulate the decay of turbulence intensity. For the present simulations, the variation of eddy viscosity ratio did not have a significant impact on the turbine loads as long as the target turbulence intensity was achieved at the rotor plane. The sensitivity of flow

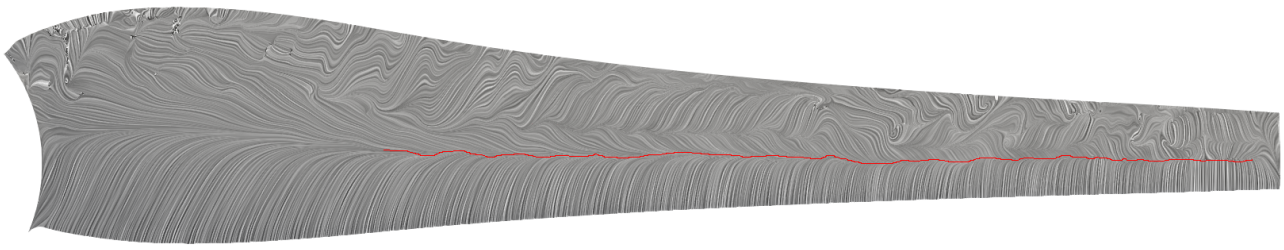

(a) *Clean* case

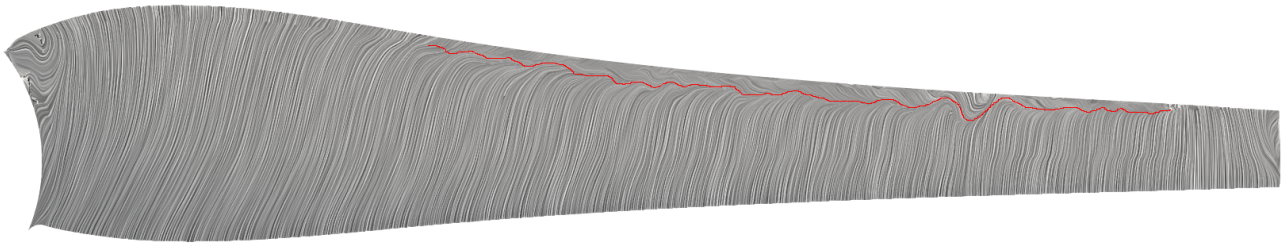

(b) *Grid* case

Fig. 12. Limiting streamlines on the suction side of the blade (leading edge down, trailing edge up)

conditions at the turbine blade to turbulence intensity could be visualized by the limiting streamlines.

The thrust coefficient showed ideal convergence behavior in the grid refinement study and a numerical uncertainty of around $5\,\%$ or less was achieved. The power coefficient did not present such a clear convergence behavior and the here determined uncertainty for C_P of around $13\,\%$ may be overestimated. An additional data point from an even finer mesh could help to achieve a more adequate fit for the extrapolation of the exact solution of C_P and lead to a smaller discretization error. Furthermore, future validation work also needs to include the experimental uncertainties to be published soon.

Even considering the uncertainties, the present simulations tend to overestimate the thrust coefficient and to underestimate the power coefficient. According to the trends observed from the uncertainty analysis, an additional mesh refinement step could help to further adjust the simulated turbine performance. A corresponding mesh would likely achieve a cell count above 50 million, which is still feasible regarding the available computational power and the relatively inexpensive steady-state calculations.

Meanwhile, it must not be forgotten that the frozen-rotor approach is a simplifying assumption of the actual experimental setup. For a complex transitional flow with separation, the steady-state method may not be adequate. In future work, it is therefore planned to model the experiments with a higher degree of fidelity, adopting a computational domain in the rectangular shape of the towing tank that matches the actual blockage ratio and boundary conditions. Therefore, also the fixed turbine support structure is to be included and the influence of the free surface has to be considered. In fact, the tip clearance to the water surface is only less than a fourth of the turbine diameter and so interaction may be expected.

The plans for future research render the frozen-rotor approach infeasible, instead the rotor motion can be modeled through sliding mesh technique. Thus the upcoming work will also be able to quantify the still insufficiently researched impact of unsteady turbine loading and push the boundaries of high-fidelity CFD capabilities.

ACKNOWLEDGEMENT

The ReFRESCO code was used within the MARIN-blueOASIS R&D cooperation agreement, Feb-2022. Furthermore, the authors would like to acknowledge the use of the IRIDIS High Performance Computing Facility.

REFERENCES

[1] P. L. Fraenkel, "Power from marine currents," *Proceedings of the Institution of Mechanical Engineers, Part A: Journal of Power and Energy*, vol. 216, no. 1, pp. 1–14, 2002.

[2] A. S. Bahaj, W. M. J. Batten, A. F. Molland, and J. R. Chaplin, *Experimental investigation into the hydrodynamic performance of marine current turbines*, ser. Sustainable energy series. University of Southampton, 2005, vol. Report 3.

[3] A. S. Bahaj, A. F. Molland, J. R. Chaplin, and W. M. J. Batten, "Power and thrust measurements of marine current turbines under various hydrodynamic flow conditions in a cavitation tunnel and a towing tank," *Renewable Energy*, vol. 32, no. 3, pp. 407–426, 2007. [Online]. Available: https://www.sciencedirect.com/science/article/pii/S0960148106000516

[4] W. M. J. Batten, A. S. Bahaj, A. F. Molland, and J. R. Chaplin, "Experimentally validated numerical method for the hydrodynamic design of horizontal axis tidal turbines," *Ocean Engineering*, vol. 34, no. 7, pp. 1013–1020, 2007. [Online]. Available: https://www.sciencedirect.com/science/article/pii/S0029801806001843

[5] S. R. Turnock, A. B. Phillips, J. Banks, and R. Nicholls-Lee, "Modelling tidal current turbine wakes using a coupled RANS-BEMT approach as a tool for analysing power capture of arrays of turbines," *Ocean Engineering*, vol. 38, no. 11, pp. 1300–1307, 2011. [Online]. Available: https://www.sciencedirect.com/science/article/pii/S0029801811001089

[6] U. Ahmed, I. Afgan, D. D. Apsley, T. Stallard, and P. K. Stansby, "CFD simulations of a full-scale tidal turbine: comparison of LES and RANS with field data," in *11th European Wave and Tidal Energy Conference (EWTEC)*, Nantes, 2015. [Online]. Available: https://research.manchester.ac.uk/en/publications/cfd-simulations-of-a-full-scale-tidal-turbine-comparison-of-les-a

[7] S. Badshah, M. Badshah, N. Hafeez, S. Jan, and Z. U. Rehman, "CFD analysis of tidal current turbine performance with different boundary conditions," *IOP Conference Series: Earth and Environmental Science*, vol. 581, no. 1, 2020. [Online]. Available: https://iopscience.iop.org/article/10.1088/1755-1315/581/1/012010

[8] M. A. Holst, O. G. Dahlhaug, and C. Faudot, "CFD Analysis of wave-induced loads on tidal turbine blades," *IEEE Journal of Oceanic Engineering*, vol. 40, no. 3, pp. 506–521, 2015.

[9] S. Draycott, A. Nambiar, B. Sellar, T. Davey, and V. Venugopal, "Assessing extreme loads on a tidal turbine using focused wave groups in energetic currents," *Renewable Energy*, vol. 135, pp. 1013–1024, 2019. [Online]. Available: https://www.sciencedirect.com/science/article/pii/S0960148118315222

[10] T. G. Scarlett and I. M. Viola, "Unsteady hydrodynamics of tidal turbine blades," *Renewable Energy*, vol. 146, pp. 843–855, 2020. [Online]. Available: https://www.sciencedirect.com/science/article/pii/S0960148119309930

[11] S. W. Tucker Harvey *et al.*, "Tidal turbine benchmarking project: Stage i - steady flow experiments," in *15th European Wave and Tidal Energy Conference*, Bilbao, 2023.

[12] R. H. J. e. a. Willden, "Tidal turbine benchmarking project: Stage i - steady flow blind predictions," in *15th European Wave and Tidal Energy Conference*, Bilbao, 2023.

[13] F. G. Schmitt, "About Boussinesq's turbulent viscosity hypothesis: historical remarks and a direct evaluation of its validity," *Comptes Rendus Mécanique*, vol. 335, no. 9, pp. 617–627, 2007. [Online]. Available: https://www.sciencedirect.com/science/article/pii/S1631072107001386

[14] F. R. Menter, M. Kuntz, and R. Langtry, "Ten years of industrial experience with the SST turbulence model," *Turbulence, Heat and Mass Transfer*, vol. 4, 2003. [Online]. Available: https://www.researchgate.net/publication/228742295_Ten_years_of_industrial_experience_with_the_SST_turbulence_model

[15] R. Lopes, E. Fernandes, L. Eça, G. Vaz, and M. Kerkvliet, "Coupling two correlation-based transition models to the KSKL eddy viscosity turbulence model," *AIAA Journal*, 2021. [Online]. Available: https://arc.aiaa.org/doi/10.2514/1.J059523

[16] R. B. Langtry and F. R. Menter, "Correlation-based transition modeling for unstructured parallelized computational fluid cynamics codes," *AIAA Journal*, vol. 47, no. 12, pp. 2894–2906, 2009. [Online]. Available: https://arc.aiaa.org/doi/10.2514/1.42362

[17] E. Fernandes, "Testing transition models with two eddy viscosity turbulence models," Master's thesis, Instituto Superior Técnico, University of Lisbon, 2019. [Online]. Available: https://fenix.tecnico.ulisboa.pt/departamentos/deec/dissertacao/1409728525632680

[18] G. Vaz, F. Jaouen, and M. Hoekstra, "Free-surface viscous flow computations: validation of URANS code FreSCo," vol. 5. American Society of Mechanical Engineers Digital Collection, Feb. 2010, pp. 425–437. [Online]. Available: https://asmedigitalcollection.asme.org/OMAE/proceedings-abstract/OMAE2009/43451/425/338909

[19] C. M. Klaij and C. Vuik, "SIMPLE-type preconditioners for cell-centered, colocated finite volume discretization of incompressible Reynolds-averaged Navier-Stokes equations," *International Journal for Numerical Methods in Fluids*, vol. 71, no. 7, pp. 830–849, 2013. [Online]. Available: https://onlinelibrary.wiley.com/doi/abs/10.1002/fld.3686

[20] R. Lopes, "Simulation of transition from laminar to turbulent regime in practical applications of incompressible flow," Ph.D. dissertation, Instituto Superior Técnico, University of Lisbon, 2021. [Online]. Available: https://scholar.tecnico.ulisboa.pt/records/bV62M9x_O_iZ4CAESvlH8UhVOY5aJAmcA-nj

[21] J. Baltazar, D. Rijpkema, and J. Falcão de Campos, "On the use of the γ-Re_{θ_t} transition model for the prediction of the propeller performance at model-scale," *Ocean Engineering*, vol. 170, pp. 6–19, 2018. [Online]. Available: https://www.sciencedirect.com/science/article/pii/S0029801818307133

[22] L. Eça and M. Hoekstra, "A procedure for the estimation of the numerical uncertainty of CFD calculations based on grid refinement studies," *Journal of Computational Physics*, vol. 262, pp. 104–130, 2014. [Online]. Available: https://www.sciencedirect.com/science/article/pii/S0021999114000278

[23] P. Crepier, "Ship resistance prediction: verification and validation exercise on unstructured grids," in *Proceedings of the VII International Conference on Computational Methods in Marine Engineering*. CIMNE, 2017, pp. 365–376. [Online]. Available: https://upcommons.upc.edu/handle/2117/331841

[24] L. Eça, R. Lopes, G. Vaz, J. Baltazar, and D. Rijpkema, "Validation exercises of mathematical models for the prediction of transitional flows," in *31st Symposium on Naval Hydrodynamics*, Monterey, CA, 2016. [Online]. Available: https://www.researchgate.net/publication/307545133_Validation_Exercises_of_Mathematical_Models_for_the_Prediction_of_Transitional_Flows

[25] R. Lopes, L. Eça, and G. Vaz, "Turbulence decay corrections for transitional flow calculations," in *22nd Numerical Towing Tank Symposium*, Tomar, 2019. [Online]. Available: https://www.researchgate.net/publication/336564264_Turbulence_Decay_Corrections_for_Transitional_Flow_Calculations

[26] L. Eça and M. Hoekstra, "Evaluation of numerical error estimation based on grid refinement studies with the method of the manufactured solutions," *Computers & Fluids*, vol. 38, pp. 1580–1591, 2009.